# Regolith evolution on the millennial timescale from combined U-Th-Ra isotopes and in situ cosmogenic 10 Be analysis in a weathering profile (Strengbach catchment, France)

Julien Ackerer, François Chabaux, Jerome van Der Woerd, Daniel Viville, Eric Pelt, Elise Kali, Catherine Lerouge, Philippe Ackerer, Raphael Di Chiara Roupert, Philippe Négrel

# Regolith evolution on the millennial timescale from combined U-Th-Ra isotopes and in situ cosmogenic $^{10}$Be analysis in a weathering profile (Strengbach catchment, France)

J. Ackerer *(1), F. Chabaux *(1), J. Van der Woerd (2), D. Viville (1), E. Pelt (1), E. Kali (2), C. Lerouge (3), P. Ackerer (1), R. di Chiara Roupert (1), P. Négrel (3).

(1) Laboratoire d'Hydrologie et de Géochimie de Strasbourg, CNRS UMR 7517, University of Strasbourg (LHyGeS, 1 rue Blessig, 67084 Strasbourg cedex, France).
(2) Institut de Physique du Globe de Strasbourg, CNRS UMR 7516, University of Strasbourg (IPGS, 5 rue René Descartes, 67084 Strasbourg cedex, France).
(3) BRGM, 3 Avenue Claude Guillemin, 45060 Orléans, France.

**Abstract : 352 words**

**Text (without acknowledgment): 6538 words**

**Corresponding Authors: fchabaux@unistra.fr, julien.ackerer2@etu.unistra.fr**

## Abstract

U-Th-Ra disequilibria, cosmogenic in situ $^{10}$Be concentrations and major and trace element concentrations have been analyzed in a 2 m-deep weathering profile sampled at the summit of the granitic Strengbach catchment (France). The data have been used to independently estimate both the long-term regolith production and denudation rates and the weathering and erosion rates. Modeling of the $^{238}$U-$^{234}$U-$^{230}$Th-$^{226}$Ra disequilibrium variations in the lower part of the profile yields a regolith production rate of 12±4 mm/kyr (30±10 T/km²/yr), while modeling of the high-resolution $^{10}$Be concentration profile leads to an exposure age of 19.7±2.2 kyr, an inherited concentration of 15,000±1,000 at/g in quartz and a mean denudation rate of 22±10 mm/kyr (37±15 T/km²/yr). The consistency between production and denudation rates suggests that, on a millennial timescale, the regolith mass balance at the summit of the catchment is close to a steady state, even if the watershed may have been impacted by Quaternary climatic changes and by recent anthropogenic perturbations (e.g., 20$^{th}$ century acid rain and recent afforestation efforts). The results also indicate that physical erosion is likely the dominant long-term process of regolith denudation in the catchment. Furthermore, the comparison of the long-term production and denudation rates and of weathering and erosion rates determined from the depth profile analyses with the current weathering and erosion rates estimated at the outlet of the watershed based on monitoring of the water chemistry and sediment fluxes suggests that physical erosion may have varied more than the chemical weathering flux during the last 150 kyr. Although very few other sites with U-series, in situ $^{10}$Be and stream monitoring data are available for comparison, the current data suggest that (1) the mass balance steady state of regolith might be commonly achieved in soil mantled landscapes and (2) physical erosion has varied much more than chemical weathering in mid-mountain catchments over the last 10-150 kyr. These results highlight the importance of the combined analysis of U-series nuclides and in situ $^{10}$Be in the same weathering profile for the determination of key geomorphic parameters, which are important to constraining landscape stability and the responses of landscapes to natural or anthropogenic forcing.



## Keywords

Regolith, weathering, denudation, U-series nuclides, in situ $^{10}$Be.

## 1- Introduction

Regolith production and denudation rates, which correspond to the rate at which bedrock is weathered into mobile regolith and removed by chemical and physical processes, are key parameters in the evaluation of landscape stability and the responses of landscapes to natural or anthropogenic forcing (e.g., Brantley et al., 2007; Banwart et al., 2011). The analytical developments made over the last decades for precisely analyzing the U-series nuclides (i.e., $^{238}U$-$^{234}U$-$^{230}Th$) in geological and environmental samples have led to the development of the study of U-series nuclides in soils and weathering profiles and to the definition of a theoretical framework for quantifying regolith production rates from the variations in radioactive disequilibria along a weathering profile (Dequincey et al., 2002; Chabaux et al., 2003, 2013; Dosseto et al., 2008, 2012; Ma et al., 2010). These studies were mainly based on the analysis of $^{238}U$-$^{234}U$-$^{230}Th$ nuclides and the use of the activity ratios ($^{234}U/^{238}U$)-($^{230}Th/^{234}U$) (activity ratios will be noted hereafter with parentheses). More recently, some studies have also included the analysis of the $^{226}Ra$ nuclide and hence the use of the ($^{226}Ra/^{230}Th$) ratio (Chabaux et al., 2013; Gontier et al., 2015). Similarly, the in situ $^{10}Be$ depth profile methodology has enabled the estimation of both exposure age and mean denudation rate from cosmogenic isotope inventories (e.g., Brown et al., 1995; Braucher et al., 2009). This approach has been widely used to constrain the ages of alluvial terraces and fans (Anderson et al., 1996; Schaller et al., 2002; Brocard et al., 2003), as well as the long-term denudation rates of regolith (Small et al., 1999; Heimsath et al., 2000; Ferrier and Kirchner, 2008; Cui et al., 2016). However, very few studies have combined a detailed analysis of U-Th-Ra isotopes with cosmogenic in situ $^{10}Be$ in a single weathering profile extending from the topsoil to the bedrock. It is the aim of this work to highlight the potential of combining these two approaches to independently constrain both production and

76 denudation rates of regolith and to show that information associated with geochemical
77 mobility can be used to discuss the long-term evolution of the regolith.

78 **2- Site presentation and sampling strategy**

79 The study is performed on the Strengbach catchment, which constitutes the "Observatoire
80 Hydrogéochimique de l'Environnement" (OHGE), one of the French critical zone
81 observatories (http://rnbv.ipgp.fr). It is a small watershed of 0.8 km² located in the Vosges
82 massif (northeastern France; Figure 1A). With altitudes ranging from 883 to 1147 m (Figures
83 1B and 1C), the current climate is mountainous-oceanic, with a mean annual rainfall and
84 temperature of 1400 mm and 6°C, respectively (Viville et al., 2012). The Vosges massif
85 experienced Pleistocene glaciations in a similar way to other central European mountains,
86 such as the Black Forest and the Bavarian Forest (Heyman et al., 2013). In accordance with
87 regional climatic studies (e.g., Leroy et al., 2000), cold conditions probably persisted at the
88 altitude of the Strengbach catchment well after the Late Glacial Maximum (LGM), and the
89 Vosges forest cover likely developed only at the onset of the Holocene. The Strengbach site
90 has been affected by anthropogenic deforestation associated with pastoralism, likely
91 beginning in the Bronze Age and lasting until the end of the 19$^{th}$ century (Etienne et al.,
92 2013). In the 20$^{th}$ century, the lower grazing pressure led to natural and artificial
93 afforestation in several places in the Vosges massif. In the Strengbach catchment, the return
94 to a densely forested cover is due to the planting of spruce stands at the beginning of the
95 20$^{th}$ century. The catchment is currently covered with a mixed spruce and beech forest
96 interspersed with small clearings. The bedrock is a base-poor late Hercynian granite and is
97 covered by a 50 to 100 cm-thick brown acidic soil (Hyperdystric Cambisol ; WRB 2006). The
98 granitic bedrock was hydrothermally overprinted, with the degree of hydrothermal

alteration decreasing from the northern to the southern part of the watershed (Fichter et al., 1998).

To investigate the recent Quaternary weathering of the granitic bedrock and the denudation rate of the soil, a sampling profile has been collected on the summit of the less hydrothermally altered part of the watershed. This location avoids the presence of colluvial deposition and corresponds to the best strategy ensuring that saprolite and soil are genetically linked to the underlying bedrock and likely formed along the main vertical weathering direction. A 2 m-deep and 3 m-wide pit was dug, and the samples were collected in the middle part of the pit front (Figure 1D). Thirty-two bulk samples of ≈5 kg each were collected along the profile with a sample every 5 cm within the soil and the saprolite and every 10 cm within the fractured bedrock. The large mass collected per sample is necessary to ensure a representative analysis of the weathering profile developed on the coarse-grained granite (Gy, 1992). For each sample in the upper part of the profile (0-100 cm), the fine fraction density was obtained by weighing a known volume of soil sampled with a steel cylinder. The proportion of blocks, defined here as coarse fragments (>10 cm), was estimated via macroscopic description and photos. The bulk density of each sample was then calculated by combining the fine fraction density and the density of blocks with respect to the proportion of blocks in the horizon. For the blocks, a constant density of 2700 kg/m$^3$ is used, on the basis of granitic bedrock density measurements. A sequential crushing and rigorous quartering process was then performed to obtain representative subsamples for mineralogical analyses by X-ray diffraction (XRD), and for geochemical and isotopic analyses.

## 3- Analytical methods

### 3.1 Mineralogical and major and trace element analysis

The determination of the sample mineralogical compositions are given in Electronic Appendix A. Six thin sections of rock samples were collected at regular intervals within the granitic bedrock (Figure 1D). Major and trace element concentrations of the samples were analyzed following the technique classically used at the LHyGeS (Strasbourg, France; e.g., Prunier et al., 2015). The quality of the analysis was checked by measuring the San Joaquin soil standard (NIST SRM 2709a). The overall uncertainty is <5 % for the major element and <10 % for the trace element concentrations (Table 1).

### 3.2 U-Th-Ra isotopes

For the U-Th-Ra analysis, each subsample consists of approximately 100 mg of 53 µm powdered bulk sample. Subsamples were weighed and spiked with both a mixed artificial $^{233}U$-$^{229}Th$ spike and a $^{228}Ra$ enriched spike to measure the isotopic ratios and U-Th-Ra concentrations by isotopic dilution, using the protocol developed in the LHyGeS (Strasbourg, France; Granet et al., 2010; Chabaux et al., 2013; Pelt et al., 2013). The powders were first digested in PFA beakers using combinations of HF, $HNO_3$, HCl, $HClO_4$ and $H_3BO_3$ acids at 100-200°C, and U, Th, and Ra were then separated and purified by ion exchange chromatography using Biorad anionic resin. U and Th isotopes were measured on a plasma mass spectrometer (MC-ICP-MS Neptune), and the $^{226}Ra$ isotope was measured on a thermal ionization mass spectrometer (TIMS Triton, Table 2). The precision and accuracy of the analyses are checked by regular analysis of liquid standards (HU1 U, IRMM036 Th and $^{228}Ra$-spike), the rock standard BCR-2 and sample replicates. The ($^{234}U/^{238}U$) activity ratio was 0.9992±0.0018 for HU1 (2σ, N=19) and the $^{232}Th/^{230}Th$ isotope ratio was 326284±2855 for IRMM036 (2σ, N=21). The ($^{234}U/^{238}U$), ($^{230}Th/^{234}U$), ($^{230}Th/^{232}Th$) and ($^{226}Ra/^{230}Th$) activity ratios for BCR-2 were 1.0028±0.0018, 1.0045±0.0104, 0.8824±0.0076 and 0.9946±0.0078 (2σ, N=2), respectively.

The mean U and Th blank concentrations were 46 pg and 157 pg, respectively, whereas the Ra concentrations were below the detection limit. These blank concentrations were all negligible compared to the measured quantities of U, Th and Ra. Inter-session standard and duplicate measurements enabled estimation of the analytical uncertainty in the calculated U-Th-Ra radioactive activity ratios. The analytical uncertainty is 0.2 % for ($^{234}U/^{238}U$), 1.5 % for ($^{230}Th/^{234}U$) and 1.7 % for ($^{226}Ra/^{230}Th$) activity ratios.

### 3.3 In situ $^{10}$Be isotope

For the in situ $^{10}$Be analysis, each subsample consists of 150 g of 250-500 µm sieved powder obtained from quartering the 2 mm crushed bulk samples. Oxides and organic matter were removed by HCl leaching, and a sequential HF dissolution was performed to remove the meteoric $^{10}$Be and obtain purified quartz (e.g., Nishiizumi et al., 1989). After addition of a $^{9}$Be carrier, the purified quartz was dissolved, and beryllium separation and purification were performed by ion exchange chromatography. After hydroxylation and targeting, the $^{10}Be/^{9}Be$ ratios were measured by accelerator mass spectrometry at ASTER (CEREGE, University of Aix-Marseille, France). The $^{10}Be/^{9}Be$ ratios of the blanks and samples are approximately $1\times10^{-15}$ and $1\times10^{-13}$, respectively The overall analytical uncertainty is <5 % for the calculated $^{10}$Be concentrations (Table 3).

## 4- Determination of the regolith production rate, denudation rate and chemical mobility

### 4.1 Regolith production rate from U-Th-Ra disequilibria

The principle of determination of the regolith production rate from the analysis of U-Th-Ra disequilibria has been detailed in previous studies (e.g., Dosseto et al., 2008, 2012; Ma et al., 2010; Chabaux et al., 2011, 2013). The approach is based on the analysis of samples collected along the main weathering direction, in the present case the vertical direction. For

samples in the weathering zone, as the time variation of nuclide mobility during water rock interactions is not known *a priori*, the time evolution of radioactive nuclides, is classically described in terms of continuous processes involving, in addition to the radioactive decay laws, loss and gain processes represented by first-order kinetic rate laws for the loss processes and zero-order kinetic rate laws for the gain processes. For the $^{238}U$-$^{234}U$-$^{230}Th$-$^{226}Ra$ system, this leads to the following equations:

$$\frac{d\,^{238}U}{dt} = f_{238}\,^{238}U_0 - k_{238}\,^{238}U - \lambda_{238}\,^{238}U \quad (1)$$

$$\frac{d\,^{234}U}{dt} = f_{234}\,^{234}U_0 + \lambda_{238}\,^{238}U - k_{234}\,^{234}U - \lambda_{234}\,^{234}U \quad (2)$$

$$\frac{d\,^{230}Th}{dt} = f_{230}\,^{230}Th_0 + \lambda_{234}\,^{234}U - k_{230}\,^{230}Th - \lambda_{230}\,^{230}Th \quad (3)$$

$$\frac{d\,^{226}Ra}{dt} = f_{226}\,^{226}Ra_0 + \lambda_{230}\,^{230}Th - k_{226}\,^{226}Ra - \lambda_{226}\,^{226}Ra \quad (4)$$

where $\lambda_i$, $k_i$ and $f_i$ are the radioactive decay, loss and gain constants (in $yr^{-1}$), respectively, for the radionuclides i (i.e., $^{238}U$, $^{234}U$, $^{230}Th$ and $^{226}Ra$). In the equations, $t$ is the time elapsed between the reference weathering state and its current state. For simplification during the equation-solving procedure, the input fluxes are expressed as a proportion of the number of atoms of nuclides added per year to the initial sample. The loss (k) and gain (f) terms used in the equations are usually assumed to be constant with time for the purpose of simplicity and tractability (e.g., Dequincey et al., 2002; Dosseto et al., 2008; Ma et al., 2010; Chabaux et al., 2013). The mean production rate of regolith, P (in mm/kyr), can be estimated through the resolution of the above equation system and the determination of the age $\Delta t$ (in kyr) of a sample relative to a reference sample from deeper in the profile at a distance $\Delta h$ (in mm)

along the weathering direction. For isovolumetric weathering, P is given by the following equation:

$$P = \frac{\Delta h}{\Delta t} \quad (5)$$

As the gain and loss coefficients in equations 1-4 are not known and the $^{238}U$-$^{234}U$-$^{230}Th$-$^{226}Ra$ analyses yield only three independent data per sample, namely the ($^{234}U/^{238}U$), ($^{230}Th/^{234}U$) and ($^{226}Ra/^{230}Th$) ratios, the analysis of only one sample (in addition to a reference sample) is not sufficient to determine the weathering production rate P. The mathematical formalism developed to retrieve such time information assumes that the gain and loss coefficients ($k_i$ and $f_i$) of the model can be considered constants, at least for a part of the profile from which several different samples can be collected and analyzed. The measured ($^{234}U/^{238}U$), ($^{230}Th/^{234}U$) and ($^{226}Ra/^{230}Th$) ratios of each sample are used to determine the mobility parameters of the model and the age of different samples relative to the reference sample. The numerical solutions are obtained using a stochastic quantum particle swarm optimization scheme (more details in Chabaux et al., 2013), which minimizes the sum of the squared differences between the measured and estimated activity ratios. The parameter solutions that allow the model to fit the observed activity ratios within 1 % error are retained and averaged to obtain a set of optimized output parameter values. The uncertainties in the parameter estimates are calculated as two-sigma standard deviations on the mean parameter estimate. It is important to stress here that such modeling approaches only give mean long-term values, i.e., over several kyr or 10 kyr, for regolith production rates and nuclide gain and loss parameters.

### 4.2 Regolith denudation rate from in situ $^{10}Be$ depth profile

As with U-series disequilibrium methodology for regolith production rate, the depth variations of in situ $^{10}$Be concentrations within a weathering profile are recognized as a powerful approach to constrain geomorphologic parameters, including the mean denudation rate of a regolith (e.g., Siame et al., 2004; Dosseto and Schaller, 2016). In situ $^{10}$Be is produced at the surface of the Earth by the interaction of cosmic rays and rock atomic nuclei (Brown et al., 1995). By taking into account (1) the different attenuation lengths of secondary neutrons and muons, which produce $^{10}$Be mainly in surface horizons for neutrons and at greater depths for muons (Kim and Englert, 2004), and (2) their relative contribution to the total produced $^{10}$Be, the depth variations of in situ $^{10}$Be concentrations within a weathering profile is given by (e.g., Siame et al., 2004; Braucher et al., 2009):

$$C(t,d,z) = C_0 \exp(-\lambda t) + \frac{P_0 * P_n}{\frac{\rho d}{K_n} + \lambda} \exp\left(\frac{-\rho z}{K_n}\right)\left(1 - \exp\left(-t(\frac{\rho d}{K_n} + \lambda)\right)\right)$$
$$+ \frac{P_0 * P_{nm}}{\frac{\rho d}{K_{nm}} + \lambda} \exp\left(\frac{-\rho z}{K_{nm}}\right)\left(1 - \exp\left(-t(\frac{\rho d}{K_{nm}} + \lambda)\right)\right)$$
$$+ \frac{P_0 * P_{fm}}{\frac{\rho d}{K_{fm}} + \lambda} \exp\left(\frac{-\rho z}{K_{fm}}\right)\left(1 - \exp\left(-t(\frac{\rho d}{K_{fm}} + \lambda)\right)\right) \quad (6)$$

where *t* is the exposure age of the profile (in yr), *d* is the mean denudation rate (in cm/yr), *z* is the depth of each sample (in cm), $C_0$ is the initial concentration from previous exposure (in atoms/g quartz), $\lambda$ is the radioactive decay of the $^{10}$Be (in yr$^{-1}$) and $\rho$ is the integrated density of each sample (in g/cm$^3$). $P_0$ is the total production rate of $^{10}$Be at the surface of the soil (12.17 at/g/yr and 0.266 at/g/yr for spallation and muons, respectively, determined with the CRONUS online calculator; Balco et al., 2008). $P_n$, $P_{nm}$ and $P_{fm}$ are the relative contributions of 97.85, 1.5 and 0.65 % to the total production and $K_n$, $K_{nm}$ and $K_{fm}$ are the effective

attenuation lengths of 150, 1500 and 5300 g/cm², for secondary neutrons, negative muons and fast muons, respectively (Braucher et al., 2009). The depth variations of in situ $^{10}$Be concentrations in a weathering profile can thus be used to estimate the exposure age and the mean denudation rate of a regolith, in addition to the inherited $^{10}$Be concentration, without any steady state assumption.

### 4.3 Chemical mobility and volumetric variation

In addition to the determination of regolith production and denudation rates from the above approaches, the chemical mobility and volumetric variation associated with the weathering processes can be estimated through the analysis of major and trace element concentrations. Based on the presence of an immobile element j, the chemical mobility of an element i during weathering can be quantified by mass transfer coefficients (Brimhall et al., 1991), as defined by the following:

$$\tau_i = \left( \frac{C(i)_{sample} * C(j)_{bedrock}}{C(i)_{bedrock} * C(j)_{sample}} - 1 \right) \quad (7)$$

where $C(i)_{sample}$ and $C(i)_{bedrock}$ represent the concentrations of the element $i$ for a given sample and for the deepest bedrock sample and $C(j)_{sample}$ and $C(j)_{bedrock}$ represent the concentrations of the immobile element j for a given sample and for the deepest bedrock sample, respectively. Positive or negative $\tau_i$ values imply the gain or loss, respectively, of the element i relative to the deepest bedrock sample, taken here as the reference rock. In addition, the chemical depletion fraction (Riebe et al., 2003), allows an estimation of the denudation fraction due to chemical weathering between the reference bedrock sample and a given sample and is defined by the following:

$$CDF = \left(1 - \frac{C(j)_{bedrock}}{C(j)_{sample}}\right) \quad (8)$$

It is also possible to estimate the relative volume variation associated with rock weathering between two considered levels by the volumetric strain index calculation (Brimhall et al., 1991; Riebe et al., 2003):

$$\varepsilon = \left(\frac{C(j)_{bedrock} * d_{bedrock}}{C(j)_{sample} * d_{sample}}\right) - 1 \quad (9)$$

where $d_{bedrock}$ and $d_{sample}$ are the bulk density values of the bedrock and the considered sample, respectively. Values of $\varepsilon$ close to zero imply isovolumetric weathering, while positive or negative values indicate expansion or compaction, respectively.

## 5- Results

### 5.1 Mineralogical and geochemical variations within the weathering profile

The whole rock XRD analyses are presented in Appendix A and in Table EA1. These data along with the thin section observations are consistent with previously published data for the Strengbach site (e.g., Fichter et al., 1998) and indicate that quartz and muscovite do not present any significant evidence of weathering in the granitic bedrock. Biotite is weathered at all depths and replaced by clays, sericite and hematite. The K-feldspar and plagioclase crystals show structural and mineralogical evolution from the base to the top of the granite, with a higher density of clay filled cracks in samples from the granite top. Carlsbad and polysynthetic twins are identifiable at the granite base, while it is more difficult to recognize them at the granite top. The analysis of the <2 μm clay fraction (Table EA1) indicates that the

263 clay composition is relatively homogeneous within the granitic bedrock and is dominated by
264 illite (40 to 60 % illite, 20 to 30 % inter-stratified illite/smectite, 5 to 25 % of smectite and 5
265 to 10 % of kaolinite). The clay composition is different and more variable in the soil, where
266 the smectite and inter-stratified clays become dominant (60 to 70 %) followed by the illite
267 (20 to 30 %) and kaolinite (5 to 10 %). These data show a significant increase in supergene
268 alteration from the base to the top of the profile, in accordance with the increase in the loss
269 on ignition (LOI, Table 1).

270 The variations in the major and trace element concentrations within the weathering profile
271 (Table 1) have been used to estimate the chemical mobility associated with weathering by
272 the calculation of the mass transfer coefficients. For this calculation, Ti is often considered
273 one of the best-suited immobile elements (e.g., Egli et al., 2006). For the tau calculation, the
274 normalization to Ti rather than to Zr concentration has been preferred, even if Zr can be
275 considered immobile in such environment (Rihs et al., 2011). The reason is the better
276 analytical precision obtained for the Ti concentrations (3%) than for Zr (≈10%), which leads
277 to a better precision of the tau value determined with Ti (≈10%) than with Zr (≈20%). The
278 calculation of relatively constant ratios within the profile between Ti and other elements
279 usually considered immobile, such as Ta (not shown) and Th (Figure 2c), especially in the
280 deeper part of the profile, reinforces the assumption that Ti is mainly immobile during
281 weathering. Tau values indicate no significant mobility for the main major elements ($Na_2O$,
282 $K_2O$, CaO, $Al_2O_3$, and $SiO_2$) in the deeper part of the granitic profile below 100 cm depth
283 (Figure 2a). The depletion becomes significant in the regolith portion above 100 cm depth,
284 with chemical mobility trends that differ from one element to another, especially in the
285 uppermost part of the soil known to be significantly affected by biological processes,
286 vegetation cycling and atmospheric deposition (e.g., Stille et al., 2011; Gangloff et al., 2014).

In this upper part of the profile, the volumetric strain index indicates a significant expansion of the soil horizons, with $\varepsilon$ values from 50 to 150 %, while deeper in the profile, in the granite and saprolite horizons, the weathering is nearly isovolumetric (Figure 3b).

As for tau values, the depth variations in the U/Th concentration ratios measured by isotopic dilution, which are more precisely estimated than the tau values, allow for subdividing the profile into two main zones, with U loss in the lower part of the profile, which gradually increases upwards up to approximately a depth of 100 cm, and a U/Th ratio increase toward the surface above 100 cm (Figure 2b). This increase might indicate Th migration due to complexation with organic colloids, as observed at other sites (Rihs et al., 2011), or U inputs from external atmospheric deposition, as suggested in other contexts (Pelt et al., 2013; Chabaux et al., 2013). Regardless of the precise origin of this increase, the U/Th data confirm that the transition between granitic bedrock and regolith at a depth of approximately 100 cm vertically divides the weathering profile into two distinct zones that are marked by different chemical mobility values and likely exhibit specific weathering processes.

### 5.2 U-Th-Ra and in situ $^{10}$Be systematics

The depth subdivision of the profile inferred from major and trace element mobility is also observed in the U-Th-Ra disequilibrium data (Table 2, Figure 4). The lower part of the profile (below 100 cm depth) is characterized by rather simple and continuous variation trends in the ($^{234}$U/$^{238}$U), ($^{230}$Th/$^{234}$U) and ($^{226}$Ra/$^{230}$Th) activity ratios with depth, with an increase in the ($^{234}$U/$^{238}$U) and ($^{230}$Th/$^{234}$U) ratios with decreasing depth and a decrease in the ($^{226}$Ra/$^{230}$Th) ratios with decreasing depth (Figure 4). In the upper regolith, the ($^{234}$U/$^{238}$U) and ($^{230}$Th/$^{234}$U) activity ratios define clearly opposite trends with depth, which support the suggestion that the two parts of the profile are marked by different weathering processes.

310 The upper part of the profile is also characterized by much more scattered ($^{226}Ra/^{230}Th$)
311 ratios, without a simple correlation with depth.

312 For in situ $^{10}Be$, the concentrations point to a progressive decrease with depth but with two
313 different patterns of variation in the profile, one in the deeper horizons, where the
314 weathering is isovolumetric, and the second one in the uppermost regolith horizons (<50
315 cm), which are affected by volumetric expansion (Table 3, Figure 3). The deeper part is
316 characterized by a common exponential decrease in $^{10}Be$, while the soil to upper regolith
317 part (0-50 cm) is characterized by a linear decrease in the in situ $^{10}Be$ concentration with
318 depth (Figure 3).

319 **6. Discussion**

320 **6.1 Determination of regolith production and denudation rates**

321 The mineralogical and geochemical data lead to a depth-dependent division of the profile
322 into two main parts, with progressive variation trends of the U-series systematic in the
323 bedrock and more scattered variations in the upper horizons (Fig. 4). Similar to the results of
324 the analyses of the short half-life $^{228}Ra$ and $^{228}Th$ nuclides in soil profiles from different forest
325 catchments, including the Strengbach (Rihs et al., 2011; Gontier et al., 2015), the short-
326 distance variations in the upper horizons most likely result from preferential Th mobility
327 related to the differential mobilization of radionuclides in the presence of organic matter. As
328 also emphasized in Gontier et al., (2015), such short-distance redistributions in the soil
329 horizons may imply significant variability of the mobility coefficients in this part of the
330 profile, at least for Th isotopes. Thus, this effect prevents the direct application of the
331 radioactive disequilibrium methodology described in section 4-1. In the Strengbach case, and
332 likely in many other forest contexts, the bedrock is thus the most suitable place to quantify

333 the mean long-term regolith production rate via the conventional U-Th-Ra methodology. In
334 the present study, the modeling approach has been therefore applied only to the lower part
335 of the profile, in which Th can be assumed to be immobile (Figure 2c), consequently reducing
336 the number of unknowns in the modeling ($k_{230}$=0 and $f_{230}$=0). The modeling results (Figure 4)
337 show that the mean U mobility parameters fall within the range of existing data for shale
338 and granodiorite lithologies (Ma et al., 2010; Dequincey et al., 2002; Dosseto et al, 2008;
339 Chabaux et al, 2013). As evidenced by the obtained coefficients, the particular positive
340 correlation between ($^{234}U/^{238}U$) and ($^{230}Th/^{234}U$) ratios in the deeper part of the profile do
341 not correspond to a simple leaching of U. To explain the ratios of ($^{234}U/^{238}U$)>1 and
342 ($^{230}Th/^{234}U$)>1, U removal must have occurred at a higher rate than U input, and incoming U,
343 which may originate from U mobilization in the upper horizons, must have been
344 characterized by a higher $^{234}U$-$^{238}U$ fractionation than the removed U (Figure 4, details also in
345 Dequincey et al., 2002). Such mobility implies precipitation of U-rich secondary minerals,
346 such as Fe-oxyhydroxides, from fluids with ratios of ($^{234}U/^{238}U$)>1. This hypothesis is
347 supported by the ratios of ($^{234}U/^{238}U$)>1 in soil solutions from a neighboring profile in the
348 same part of the watershed (Prunier et al., 2015). The U-Th-Ra modeling also gives the
349 elapsed time between the granite base and the lower regolith, which yields a mean regolith
350 production rate of 12±4 mm/kyr. Considering the density of 2.5 for the lower regolith, the
351 regolith production rate in terms of specific flux is 30±10 T/km²/yr.

352 For application of the in situ $^{10}Be$ approach (section 4-2), a numerical inverse procedure has
353 been used to determine the exposure age, the mean denudation rate and the inherited
354 concentration that best explain the data from equation 6. The inverse procedure consists of
355 minimizing the chi-square value of the system by the algorithm of Levenberg-Marquardt

(Marquardt, 1963) and has been adapted to take into account the volumetric expansion of the upper regolith. The chi-square value is defined as follows:

$$X = \sum \left( \frac{C_{data}\,(z) - (C_{model}(t, d, C_0, z) + \Delta C)}{\sigma(z)} \right)^2 \quad (10)$$

where $C_{data}(z)$ and $C_{model}(t, d, C_0, z)$ are the measured and modeled $^{10}$Be concentrations, respectively, and $\sigma(z)$ is the uncertainty in the measured $^{10}$Be concentration for a sample at depth $z$. A correction factor $\Delta C$ has been introduced to take into account the volumetric expansion of the upper 50 cm because the density variation only is insufficient to explain the concentration trend of this part of the profile. This implies that expansion must have occurred relatively late (<5–10 kyr) in the history of the profile, as the measured concentrations do not reflect the corresponding production rate changes. Uncertainty in the parameters is estimated from the covariance matrix of the problem. It is important to stress that, considering the mean denudation and the surface $^{10}$Be production rates at the summit of the Strengbach watershed, the current accumulation of $^{10}$Be within the profile is not balanced by erosion and radioactive decay. Because a $^{10}$Be concentration steady state is not present, the geochronometric application of the modeling is possible. The best fit gives an exposure age of the profile of 19,734±2,168 yr, a mean denudation rate of 22±10 mm/kyr (in terms of specific flux, 37±15 T/km²/yr, based on the mean density of the regolith of 1.7) and an inherited $^{10}$Be concentration of 15,000±1,000 at/g quartz (Figure 3).

### 6.2 Implications for regolith evolution on the millennial timescale

To the best of our knowledge, this study is likely the first one to combine U-series and in situ $^{10}$Be analyses on the same samples in a single weathering profile with such a depth extent

and spatial resolution. This coupled approach allows for determining, in addition to the regolith denudation and production rates, the exposure age of the profile and the potential $^{10}$Be inherited concentration. As illustrated in the following, these estimates are relevant for recovering the Quaternary dynamics of the weathering profile.

The determined exposure age inferred from the $^{10}$Be data indicates the occurrence of an erosive event at the summit of the Strengbach watershed approximately 20,000 yr ago, likely resulting from glacial or peri-glacial processes in relation with the last Würm glaciation, which is in accordance with regional investigations (Seret et al., 1990; Mercier et al., 1999). In addition, the occurrence of an inherited $^{10}$Be concentration within the bedrock indicates a complex erosive history at the summit of the Strengbach catchment. By extrapolating the long-term regolith propagation rate determined from U-Th-Ra variations (i.e., 30±10 T/km²/yr or 12±4 mm/kyr), an age of approximately 150 kyr is obtained for the entire 2 m-thick profile analyzed in this study. This age would lead to a $^{10}$Be concentration at 2 m depth much higher than the inherited $^{10}$Be concentration of 15,000 at/g quartz obtained from our data. In this bedrock, the measured inherited $^{10}$Be concentration corresponds to the concentration obtained from a muonic exposure at approximately 4 m depth over ≈150 kyr. A way to reconcile all the data, assuming the above determined average denudation rate of 22 mm/kyr, is that a thickness of 2 m was eroded 20 kyr ago and that a total resetting of the bedrock $^{10}$Be inventory must have occurred 150 kyr ago, which is consistent with the fact that the penultimate Riss glaciation was probably more intense than the last Würm glaciation in the mountains of central Europe (Dehnert et al., 2010).

The independent determination of regolith production and denudation rates from U-Th-Ra isotopes and in situ $^{10}$Be constitutes an interesting method for discussing the stability state

of a weathering profile on a millennial timescale. For the Strengbach case, the proposed approach gives similar values for denudation rate (37±15 T/km²/yr) and production rate (30±10 T/km²/yr), suggesting that at a millennial time scale, the regolith mass balance at the summit of the catchment is close to steady state, even if it was perturbed 20 kyr ago. Such a conclusion may indicate that the return to mass balance steady state is relatively fast in this system, i.e., obtained in less than 20 kyr and/or that the erosive event that occurred 20 kyr ago has only very transiently disturbed the processes controlling regolith formation at the summit of the Strengbach watershed. The results may also suggest that the recent anthropogenic perturbations linked to the 20$^{th}$ century, e.g., acid rain or the recent afforestation efforts, which may have recently modified the cationic concentrations and acidity of soil and stream waters in the watershed (Viville et al., 2012; Prunier et al., 2015), have not perturbed the $^{10}$Be and U-Th-Ra long-term records.

Very few other studies combining U-series disequilibrium and cosmonuclides methodology exist for other sites, even when including those involving the meteoritic $^{10}$Be approach (Table 4). In addition, these other studies usually dealt with more superficial regolith and different sample sets for isotopic analyses. However, despite these limitations, the data indicate that in all the investigated mid-mountain catchments, which are characterized by different climatic and tectonic settings, there is a fairly good consistency between the long-term regolith production and denudation rates (Table 4). This seems to be especially true at the ridge-tops and/or hill-crests of watersheds, where geochronological interpretations are likely less affected by colluvial transport and deposition. Altogether, even if such a conclusion remains preliminary, the current data suggest that the long-term regolith evolution could be commonly at steady state.

### 6.3 Comparison of millennial and present-day weathering and erosion rates

Because U-series and $^{10}$Be approaches integrate long-term processes, a substantial step to understand the recent regolith evolution could be provided by the comparison of long-term weathering and erosion rates with present-day estimates. As established by Riebe et al. (2003), the knowledge of denudation rates determined by cosmogenic nuclide, combined with the geochemical mass balance approaches and the definition of the chemical depletion fraction (CDF), allow to distinguish the chemical and physical components of the total denudation. This approach is predicated on an assumption of steady state, which is supported by the consistency between U-series and $^{10}$Be results. The total weathering rate in T/km²/yr is as follows:

$$W = D\left(1 - \frac{\mathrm{C(Ti)}_{rock}}{C(Ti)_{soil}}\right) = D \times CDF \quad (11)$$

where D is the mean denudation rate in T/km²/yr inferred from the cosmogenic $^{10}$Be and $C(Ti)_{rock}$ and $C(Ti)_{soil}$ are the concentrations of titanium (considered an immobile element) in the bedrock and in the soil, respectively. The application of this approach to the bedrock and the soil levels of the studied weathering profile leads to a CDF value of 0.22 when using for the average Ti concentrations of the bedrock and soil levels. A maximum CDF value of 0.30 is obtained by using the lowest Ti concentrations measured in the bedrock and the highest concentrations in the soil. Similar calculations can be made with Zr, which can also be considered an immobile element in the Strengbach catchment (Rihs et al., 2011): CDF values between 0.13 and 0.25 are obtained according to whether the average concentration values or the extreme values are used for each level. These different

calculations indicate that at the profile scale, long-term chemical weathering accounts for 13 to 30 % of the total denudation, which yields a long-term chemical weathering flux of between 5 and 11 T/km²/yr and consequently a long-term erosion flux of between 26 and 32 T/km²/yr. Therefore, physical erosion is the main process controlling the loss of regolith.

The above weathering flux calculations can be easily adapted to calculate the long-term weathering flux of a specific chemical element by using the mean denudation rate ($D$), the elemental concentrations within the bedrock ($C(x)_{bedrock}$) and the tau values ($\tau_x$) in the upper soil (Riebe et al., 2003):

$$W_x = D * C(x)_{bedrock} * (-\tau_x) \quad (12)$$

Based on this approach, long-term weathering fluxes of approximately 3 ± 2 T/km²/yr for Si and 0.7 ± 0.47 T/km²/yr for cations can be estimated from the geochemical variations along the regolith profile at the watershed summit. Similarly, the regular analyses of the dissolved fluxes and the sediment loads carried by the Strengbach stream allow for estimation of the current erosion and weathering rates at the watershed scale. The combination of the suspended and bed load monitoring yields a total erosion rate of 5 ± 1 T/km²/yr at the watershed outlet (Viville et al., 2012). By correcting the net flux for basic cations from atmospheric deposition, a cationic weathering flux of 1.98 ± 0.2 T/km²/yr and a Si weathering flux of 2.89 ± 0.3 T/km²/yr are estimated (Viville et al., 2012). The current exported flux for Si determined at the watershed outlet is surprisingly very close to the long-term Si weathering flux associated with regolith formation inferred for the watershed summit. This consistency means that the first-order chemical weathering, which is controlled by the rates of primary mineral dissolution and secondary mineral precipitation, is rather

466 spatially uniform and stable in time. In contrast, the current cationic flux in the Strengbach
467 stream seems to be higher than the long-term flux determined at the profile scale for basic
468 cations. This difference may be due to a recent increase in basic cation leaching from
469 Strengbach soils, possibly triggered by the acidic atmospheric inputs and/or the forest
470 management evolution experienced by the Strengbach catchment in recent decades (Viville
471 et al., 2012; Prunier et al., 2015). In contrast to the weathering rates, the long-term erosion
472 rate determined from $^{10}$Be and CDF data (approximately 30 T/km²/yr) is clearly higher than
473 the current erosion rate determined in the Strengbach stream (approximately 5 T/km²/yr;
474 Viville et al., 2012). The latter value is certainly an underestimate, as the suspended load was
475 sampled only once every one or two weeks, which probably does not allow for a correct
476 estimate of the suspended load exported during flood events. A more recent study of the
477 erosion fluxes exported from the Strengbach watershed at its outlet, including an accurate
478 determination of the suspended load exported from the watershed during flood events,
479 yielded an erosion rate no higher than 10 T/km²/yr (Cotel et al., 2016). Regarding the
480 sampling frequency developed in the latter study, and even if the bed load is always difficult
481 to estimate precisely, an additional bias for the current erosion rates by a factor of three
482 seems improbable. Thus, unlike weathering fluxes, the long-term erosion rate determined at
483 the watershed summit and the present-day rate at the watershed scale are most likely
484 different. Such a discrepancy is certainly not surprising, and can result from spatial
485 heterogeneity in the erosion rate at the watershed scale, with high erosion rates along the
486 main crests possibly counterbalanced by sediment storage downhill. It could also result from
487 temporal variability in the physical erosion rate, with, for instance, high erosion rates during
488 cold conditions, probably persisting long after the LGM, followed by lower erosion rates due

489 to stabilization of the regolith by soil and vegetation cover development during the
490 Holocene.

491 As illustrated in the Strengbach case, this combination of U-series, in situ $^{10}$Be and stream
492 monitoring allows for discussing the weathering and erosion variability at different spatial
493 and temporal scales. Another site where a similar comparison is possible is the Rio Icacos
494 watershed (Table 5 in Chabaux et al., 2013). Similar to the Strengbach catchment, an analysis
495 suggests relatively similar long-term and short-term weathering rates, whereas significant
496 differences exist between long-term denudation rates inferred from $^{10}$Be data and current
497 erosion rates determined from sediment monitoring, which is also similar to the Strengbach
498 catchment (Table 4). However, in this case, unlike the Strengbach catchment, the current
499 erosion rates are higher than the long-term ones. This large variability in the physical erosion
500 fluxes through time is also suggested in a few other studies. In the Susquehanna Shale Hills
501 Observatory, it has been proposed that current erosion rates may be lower than previous
502 conditions because deep sediments in the valley floor appear to retain a record of enhanced
503 colluvial transport in the past (West et al., 2013). In Australia, longer sediment residence
504 times have been proposed for the Murrumbidgee River during warm periods, in association
505 with the development of vegetation cover and a decrease in erosion (in Dosseto and
506 Schaller, 2016). Even if, once again, there are very few sites where long-term trends are
507 compared to short-term trends, it seems that mid-mountain watersheds that experienced
508 glacial or periglacial conditions during the LGM (Strengbach, SSHO or Australian upper
509 watersheds) recorded a decrease in erosion rates with the onset of Holocene. In contrast, in
510 the Rio Icacos watershed, characterized by warmer conditions and hence unaffected by
511 periglacial processes, the current erosion rates are faster (Table 4). Thus, the above data
512 support the assumption deduced from the Strengbach case that the erosion rates have been

513 more variable than the chemical weathering rates during the Quaternary. The data might
514 also suggest a possible role of periglacial processes in the erosional response to Quaternary
515 climatic variations.

516 **7 Conclusions**

517 The study performed on a weathering profile sampled at the summit of the Strengbach
518 catchment illustrates the interesting results of the combined analyses of in situ $^{10}Be$
519 concentrations, $^{238}U$-$^{234}U$-$^{230}Th$-$^{226}Ra$ disequilibria and major and trace element
520 concentrations. As summarized in Figure 5, this combination is a powerful methodology for
521 recovering key parameters of the long-term regolith evolution. This approach suggests that
522 the long-term regolith evolution in the Strengbach watershed is relatively close to steady
523 state, despite recent anthropogenic perturbations. In addition, in regard to the mineralogical
524 properties of the profile and implicit assumptions of the U-Th-Ra modeling, it appears that in
525 this site (as well as in many other forest contexts), the bedrock is the most suitable place to
526 quantify the regolith production rate using the U-Th-Ra methodology. The results also
527 highlight the importance of having a sufficiently dense sampling strategy along the regolith
528 depth profile to recover the Quaternary polyphase history of the regolith from the analysis
529 and modeling of in situ $^{10}Be$. In combination with the above data, geochemical and mass
530 balance calculations performed in the Strengbach stream and along the weathering profile
531 allow for investigating the regolith evolution at different spatial and temporal scales. The
532 results indicate that physical erosion is the dominant process of regolith loss in the
533 Strengbach catchment and has probably varied much more than chemical weathering
534 through time. Although very few sites with U-series, in situ $^{10}Be$ and stream monitoring data
535 are available for comparison, the current data suggest that (1) mass balance steady state of

regolith can be commonly achieved in soil mantled landscapes and (2) physical erosion has exhibited higher variability than chemical weathering over the last 10-150 kyr. The combined U-series and in situ $^{10}$Be analyses in high spatial resolution depth profiles could become a powerful approach in the future for providing new quantitative insights on weathering profile dynamics and regolith erosive history over Holocene and Late Pleistocene time periods. The association of these approaches with the monitoring of water chemistry and sediment fluxes at watershed outlets seems also important to correctly positioning the present-day erosion and weathering rates relative to the past rates recorded by the U-Th-Ra and in situ $^{10}$Be inventories.

## Acknowledgments

This work has been supported by the funding of a Ph.D. scholarship to J. Ackerer from the Region Alsace, France and the BRGM, Orléans, France. $^{10}$Be ratios were measured at the ASTER AMS national facility (CEREGE, Aix-en-Provence), supported by INSU-CNRS, IRD and CEA. This study was financially supported by funding from the REALISE program to F. Chabaux. We are grateful to A. Aubert and N. Maubec for the X-ray diffraction measurements and interpretations and to R. Boutin for the analysis of the major and trace element concentrations. We also thank M. Granet and T. Perrone for their help during sample preparation and P. Stille, M.C. Pierret and C. Bosia for discussions during the course of the work. We sincerely thank S. Brown and two anonymous reviewers, as well as the Editor D. Vance, for their very constructive and thoughtful comments. This is a LHyGeS-EOST contribution.

## Table and figure captions

Table 1: Some chemical and physical characteristics of the studied weathering profile. Major and trace element concentrations were determined by conventional tetraborate alkaline fusion followed by mass spectrometry and atomic emission spectrometry measurements (ICP-MS and ICP-AES procedure) (uncertainty <5 % for major element and <10 % for trace element concentrations). STR13-53$^2$ is a dissolution powder duplicate. STR13-53$^3$ is a quartering duplicate that encompasses the whole crushing process.

564 Table 2: U-series data. U and Th concentrations are calculated from isotopic dilution. The
565 uncertainties are at the 2σ level: 0.2 % and 0.5 % for U and Th concentrations, 0.2 % for ($^{234}U$ /$^{238}U$), 1
566 % for ($^{230}Th$ /$^{232}Th$), 1.5 % for ($^{230}Th$ /$^{234}U$) and 1.7 % for ($^{226}Ra$/$^{230}Th$) activity ratios. STR13-53$^{2}$ is a
567 dissolution powder duplicate. STR13-53$^{3}$ is a quartering duplicate that encompasses the whole
568 crushing process. For the activity ratio calculation, the following radioactivity constants were used:
569 $\lambda_{232}=4.948\times10^{-11}\,yr^{-1}$, $\lambda_{230}=9.158\times10^{-6}\,yr^{-1}$, $\lambda_{234}=2.826\times10^{-6}\,yr^{-1}$, $\lambda_{238}=1.551\times10^{-10}\,yr^{-1}$, and $\lambda_{226}=4.335\times10^{-}$
570 $^{4}\,yr^{-1}$ (Akovali, 1996; Cheng et al., 2000).

571 Table 3: In situ $^{10}Be$ data for the studied weathering profile. The elevation is 1147 m a.s.l. The latitude
572 and longitude are 48°12'29.4"N and 7°11'30.3"E, respectively. There is no shielding correction due to
573 the summit location of the profile. The surface production rates were determined with the CRONUS
574 online calculator (Balco et al., 2008) and are 12.17 at/g/yr and 0.266 at/g/yr for spallation and
575 muons, respectively. The total $^{9}Be$ represents the carrier and natural $^{9}Be$ of the samples (ICP-AES
576 measurements). AMS analysis calibration was performed with a BeO NIST 4325 standard at ASTER.
577 $^{10}Be/^{9}Be$ are blank corrected values. Uncertainties include AMS analysis, carrier mass and blank
578 uncertainties.
579
580 Table 4: Synthesis table of the studied sites that allow for U-series and $^{10}Be$ results comparison.
581 When rates are not provided in T/km²/yr, conversions from mm/kyr to T/km²/yr have been
582 performed by assuming a regolith bulk mean density of 1700 kg/m$^{3}$. (1) This study. (2) Cotel et al.,
583 2016. (3) Ma et al., 2010. (4) West et al., 2013. (5) Jin et al., 2010. (6) Schoonejans et al., 2016. (7) Dosseto
584 et al., 2008. (8) Heimsath et al., 2000. (9) Chabaux et al., 2013. (10) Brown et al., 1995. (11) McDowell and
585 Asbury, 1994. $^{10}Be$ denudation rates have been determined by in situ $^{10}Be$ data, except for West et
586 al., 2013, where meteoritic $^{10}Be$ has been used.

587 Figure 1: a) Regional map of the Vosges massif and location of the Strengbach catchment. b) Contour
588 of the Strengbach watershed. c) Topographic map of the Strengbach watershed and location of the

589 studied weathering profile (map from OHGE). d) Sampling of the weathering profile. The pedological
590 observation led to division of the weathering profile into 3 zones: the soil from 0 to 50 cm, the
591 saprolite from 50 to 100 cm and the granitic weathered bedrock from 100 to 200 cm. Each box in the
592 column represents a collected sample. Red and blue dots indicate samples for which isotopic U-Th-Ra
593 and in situ $^{10}$Be analyses have been performed, respectively. Green dots indicate samples for which
594 thin sections have been performed.

595 Figure 2: a) Mass transfer coefficients calculated from equation 7. The uncertainty is calculated from
596 elemental concentration uncertainty propagation and is <20 % (error bars show 20 % level). b) U/Th
597 ratio. The U and Th concentrations are calculated from isotopic dilution. The uncertainty is 0.2 % for
598 U, 0.5 % for Th and is within size point. c) Th/Ti ratio. The Ti and Th concentrations are calculated
599 from alkaline fusion. The uncertainty is <15 % (error bars show 15 % level).

600 Figure 3: a) Bulk density calculated by combining the fine fraction density and the density of blocks
601 with respect to the proportion of blocks in each horizon. For the bedrock and the blocks of granite, a
602 constant density of 2700 kg/m$^3$ is assumed. b) Volumetric strain index calculated from equation 9.
603 Uncertainty is calculated from elemental concentration uncertainty propagation and is <10 % (error
604 bars show 10 % level) c) $^{10}$Be depth profile. In blue: measured $^{10}$Be concentrations. Uncertainty is <5
605 % (error bars show 5 % level). In red: best fit obtained from optimization by Levenberg-Marquardt
606 algorithm. In grey: modeled $^{10}$Be concentrations without taking into account soil expansion.

607 Figure 4: ($^{234}$U/$^{238}$U), ($^{230}$Th/$^{234}$U) and ($^{226}$Ra/$^{230}$Th) radioactive activity ratios along the weathering
608 profile. In blue: experimental data. The uncertainties are at the 2σ level: 0.2 % for ($^{234}$U /$^{238}$U), 1.5 %
609 for ($^{230}$Th /$^{234}$U) and 1.7 % for ($^{226}$Ra/$^{230}$Th) measured activity ratios. In red: best fit obtained from
610 numerical optimization. Calculated coefficients: $\mathrm{k}_{238} = 4.81 * 10^{-6} \pm 3.68 * 10^{-7}$, $\mathrm{k}_{234} = 5.47 *$
611 $10^{-6} \pm 9.20 * 10^{-7}$, $\mathrm{k}_{226} = 2.22 * 10^{-5} \pm 4.44 * 10^{-6}$, $\mathrm{f}_{238} = 1.63 * 10^{-6} \pm 4.00 * 10^{-7}$, $\mathrm{f}_{234} =$
612 $2.76 * 10^{-6} \pm 8.96 * 10^{-7}$ and $\mathrm{f}_{226} = 6.61 * 10^{-6} \pm 2.20 * 10^{-6}$ (2σ level, expressed in $\mathrm{yr}^{-1}$).
613 Calculated weathering age is approximately 69,000 yr for the modeled section.

614 Figure 5: Summary of the methodologies applied to the regolith profile at the Strengbach catchment
615 summit. Combined approaches allow for constraining the long-term evolution of the profile with
616 comparison of both regolith production and denudation rates.
617

618 **References**


619 Akovali, Y. A. (1996). Nuclear data sheets for A= 226. *Nuclear Data Sheets*, *77*(2), 433-470.

620 Anderson, R. S., Repka, J. L., & Dick, G. S. (1996). Explicit treatment of inheritance in dating
621 depositional surfaces using in situ 10Be and 26Al. *Geology*, *24*(1), 47-51.

622 Balco, G., Stone, J. O., Lifton, N. A., & Dunai, T. J. (2008). A complete and easily accessible
623 means of calculating surface exposure ages or erosion rates from 10 Be and 26 Al
624 measurements. *Quaternary geochronology*, *3*(3), 174-195.

625 Banwart, S., Bernasconi, S. M., Bloem, J., Blum, W., Brandao, M., Brantley, S., ... & Zhang, B.
626 (2011). Soil processes and functions in critical zone observatories: hypotheses and
627 experimental design. *Vadose Zone Journal*, *10*(3), 974-987.

628 Brantley, S. L., Goldhaber, M. B., & Ragnarsdottir, K. V. (2007). Crossing disciplines and scales
629 to understand the critical zone. *Elements*, *3*(5), 307-314.

630 Braucher, R., Del Castillo, P., Siame, L., Hidy, A. J., & Bourlès, D. L. (2009). Determination of
631 both exposure time and denudation rate from an in situ-produced 10 Be depth
632 profile: a mathematical proof of uniqueness. Model sensitivity and applications to
633 natural cases. *Quaternary Geochronology*, *4*(1), 56-67.

634 Brimhall, G. H., Ford, C., Bratt, J., Taylor, G., & Warin, O. (1991). Quantitative geochemical
635 approach to pedogenesis: importance of parent material reduction, volumetric
636 expansion, and eolian influx in lateritization. *Geoderma*, *51*(1), 51-91.

637 Brocard, G. Y., Van Der Beek, P. A., Bourlès, D. L., Siame, L. L., & Mugnier, J. L. (2003). Long-
638 term fluvial incision rates and postglacial river relaxation time in the French Western
639 Alps from 10 Be dating of alluvial terraces with assessment of inheritance, soil
640 development and wind ablation effects. *Earth and Planetary Science Letters*, *209*(1),
641 197-214.

642 Brown, E. T., Stallard, R. F., Larsen, M. C., Raisbeck, G. M., & Yiou, F. (1995). Denudation rates
643 determined from the accumulation of in situ-produced 10 Be in the Luquillo
644 Experimental Forest, Puerto Rico. *Earth and Planetary Science Letters*, *129*(1), 193-
645 202.
646 Chabaux F., Riotte J., Dequincey O. (2003). U-Th-Ra fractionation during weathering and river
647 transport, *Rev Mineral. Geochem., 52*, 533-576.
648 Chabaux, F., Ma, L., Stille, P., Pelt, E., Granet, M., Lemarchand, D., ... & Brantley, S. L. (2011).
649 Determination of chemical weathering rates from U series nuclides in soils and
650 weathering profiles: Principles, applications and limitations. *Applied Geochemistry*,
651 *26*, S20-S23.
652 Chabaux, F., Blaes, E., Stille, P., di Chiara Roupert, R., Pelt, E., Dosseto, A., ... & Brantley, S. L.
653 (2013). Regolith formation rate from U-series nuclides: Implications from the study of
654 a spheroidal weathering profile in the Rio Icacos watershed (Puerto Rico). *Geochimica*
655 *et Cosmochimica Acta*, *100*, 73-95.
656 Cheng, H., Edwards, R. L., Hoff, J., Gallup, C. D., Richards, D. A., & Asmerom, Y. (2000). The
657 half-lives of uranium-234 and thorium-230. *Chemical Geology*, *169*(1), 17-33.
658 Cotel S., Viville D., Pierret M.C., Benarioumlil S., Chabaux F. (2016) Evaluation of fluxes of
659 suspended matters and bedload in the small granitic Strengbach catchment (Vosges
660 massif, France). Geophysical Research Abstracts Vol. 18, EGU2016-13179.
661 Cui L., Liu C.Q., Xu S., Zhao Z.-Q., Liu T.-Z., Liu W.-J., Zhang Z.-J. (2016) Subtropical
662 denudation rates of granitic regolith along a hill ridge in Longnan, SE China derived
663 from cosmogenic nuclides depth-profiles, Journal of Asian Earth Sciences 117, 146-
664 152

665 Dehnert, A., Preusser, F., Kramers, J. D., Akcar, N., Kubik, P. W., Reber, R., & Schluechter, C.
666 (2010). A multi-dating approach applied to proglacial sediments attributed to the
667 Most Extensive Glaciation of the Swiss Alps. *Boreas*, *39*(3), 620-632.
668 Dequincey, O., Chabaux, F., Clauer, N., Sigmarsson, O., Liewig, N., & Leprun, J. C. (2002).
669 Chemical mobilizations in laterites: evidence from trace elements and 238 U-234 U-
670 230 Th disequilibria. *Geochimica et Cosmochimica Acta*, *66*(7), 1197-1210.
671 Dosseto, A., Turner, S. P., & Chappell, J. (2008). The evolution of weathering profiles through
672 time: new insights from uranium-series isotopes. *Earth and Planetary Science Letters*,
673 *274*(3), 359-371.
674 Dosseto A., Buss H. and Suresh P. O. (2012) Rapid regolith formation over volcanic bedrock
675 and implications for land-scape evolution. Earth Planet. Sci. Lett. 337, 47–55.
676 Dosseto, A., & Schaller, M. (2016). The erosion response to Quaternary climate change
677 quantified using uranium isotopes and in situ-produced cosmogenic nuclides. *Earth-*
678 *Science Reviews*, *155*, 60-81.
679 Egli, M., Mirabella, A., Sartori, G., Zanelli, R., & Bischof, S. (2006). Effect of north and south
680 exposure on weathering rates and clay mineral formation in Alpine soils. *Catena*,
681 *67*(3), 155-174.
682 Etienne, D., Ruffaldi, P., Dupouey, J. L., Georges-Leroy, M., Ritz, F., & Dambrine, E. (2013).
683 Searching for ancient forests: A 2000 year history of land use in northeastern French
684 forests deduced from the pollen compositions of closed depressions. *The Holocene*,
685 *23*(5), 678-691.
686 Fichter, J., Turpault, M. P., Dambrine, E., & Ranger, J. (1998). Mineral evolution of acid forest
687 soils in the Strengbach catchment (Vosges mountains, NE France). *Geoderma*, *82*(4),
688 315-340.

689 Ferrier, K. L., & Kirchner, J. W. (2008). Effects of physical erosion on chemical denudation
690 rates: a numerical modeling study of soil-mantled hillslopes. *Earth and Planetary*
691 *Science Letters*, *272*(3), 591-599.
692 Gangloff S., Stille P., Pierret M-C., Weber T., Chabaux F. (2014) Characterization and
693 evolution of dissolved organic matter in acidic forest soil and its impact on the
694 mobility of major and trace elements (case of the Strengbach watershed) Geochimica
695 et Cosmochimica Acta, 130, 21-41.
696 Gontier, A., Rihs, S., Chabaux, F., Lemarchand, D., Pelt, E., Turpault, M.-P. (2015) Lack of
697 bedrock grain size influence on the soil production rate, Geochimica et Cosmochimica
698 Acta, 166, 146-164.
699 Granet, M., Chabaux, F., Stille, P., Dosseto, A., France-Lanord, C., & Blaes, E. (2010). U-series
700 disequilibria in suspended river sediments and implication for sediment transfer time
701 in alluvial plains: the case of the Himalayan rivers. *Geochimica et Cosmochimica Acta*,
702 *74*(10), 2851-2865.
703 *Gy, P. M. (1992). Sampling of heterogeneous and dynamic material systems: theories of*
704 *heterogeneity, sampling and homogenizing. Elsevier.*
705 Heimsath, A. M., Chappell, J., Dietrich, W. E., Nishiizumi, K., & Finkel, R. C. (2000). Soil
706 production on a retreating escarpment in southeastern Australia. *Geology*, *28*(9),
707 787-790.
708 Heyman, B. M., Heyman, J., Fickert, T., & Harbor, J. M. (2013). Paleo-climate of the central
709 European uplands during the last glacial maximum based on glacier mass-balance
710 modeling. *Quaternary Research*, *79*(1), 49-54.
711 Jin, L., Ravella, R., Ketchum, B., Bierman, P. R., Heaney, P., White, T., & Brantley, S. L. (2010).
712 Mineral weathering and elemental transport during hillslope evolution at the

713 Susquehanna/Shale Hills Critical Zone Observatory. *Geochimica et Cosmochimica*
714 *Acta*, *74*(13), 3669-3691.
715 Kim, K. J., & Englert, P. A. J. (2004). Profiles of in situ 10 Be and 26 Al at great depths at the
716 Macraes Flat, East Otago, New Zealand. *Earth and Planetary Science Letters*, *223*(1),
717 113-126.
718 Leroy, S. A. G., ZOLITSCHKA, B., NEGENDANK, J. F., & Seret, G. U. Y. (2000). Palynological
719 analyses in the laminated sediment of Lake Holzmaar (Eifel, Germany): duration of
720 Lateglacial and Preboreal biozones. *Boreas*, *29*(1), 52-71.
721 Ma, L., Chabaux, F., Pelt, E., Blaes, E., Jin, L., & Brantley, S. (2010). Regolith production rates
722 calculated with uranium-series isotopes at Susquehanna/Shale Hills Critical Zone
723 Observatory. *Earth and Planetary Science Letters*, *297*(1), 211-225.
724 Marquardt, D. W. (1963). An algorithm for least-squares estimation of nonlinear parameters.
725 *Journal of the Society for Industrial & Applied Mathematics*, *11*(2), 431-441.
726 McDowell, W. H., & Asbury, C. E. (1994). Export of carbon, nitrogen, and major ions from
727 three tropical montane watersheds. *Limnology and oceanography*, *39*(1), 111-125.
728 Mercier, J. L., Bourlès, D. L., Kalvoda, J., Braucher, R., & Paschen, A. (1999). Deglaciation of
729 the Vosges dated using 10Be. *Acta Universitatis Carolinae–Geographica*, *2*, 139-155.
730 Nishiizumi, K., Winterer, E. L., Kohl, C. P., Klein, J., Middleton, R., Lal, D., & Arnold, J. R.
731 (1989). Cosmic ray production rates of 10Be and 26Al in quartz from glacially polished
732 rocks. *Journal of Geophysical Research: Solid Earth (1978–2012)*, *94*(B12), 17907-
733 17915.
734 Pelt, E., Chabaux, F., Stille, P., Innocent, C., Ghaleb, B., Gérard, M., & Guntzer, F. (2013).
735 Atmospheric dust contribution to the budget of U-series nuclides in soils from the
736 Mount Cameroon volcano. *Chemical Geology*, *341*, 147-157.

737 Prunier J., Chabaux F., Stille P., Pierret MC, Viville D., Gangloff S. (2015) Monitoring of
738 geochemical and isotopic (Sr,U) signatures in soil solutions for the evaluation of soil
739 weathering evolution (the Strengbach case) *Chemical Geology, 417*, 289–305.
740 Riebe, C. S., Kirchner, J. W., & Finkel, R. C. (2003). Long-term rates of chemical weathering
741 and physical erosion from cosmogenic nuclides and geochemical mass balance.
742 *Geochimica et Cosmochimica Acta*, *67*(22), 4411-4427.
743 Rihs, S., Prunier, J., Thien, B., Lemarchand, D., Pierret, M. C., & Chabaux, F. (2011). Using
744 short-lived nuclides of the U-and Th-series to probe the kinetics of colloid migration
745 in forested soils. *Geochimica et Cosmochimica Acta*, *75*(23), 7707-7724.
746 Schaller, M., Von Blanckenburg, F., Veldkamp, A., Tebbens, L. A., Hovius, N., & Kubik, P. W.
747 (2002). A 30 000 yr record of erosion rates from cosmogenic 10 Be in Middle
748 European river terraces. *Earth and Planetary Science Letters*, *204*(1), 307-320.
749 Schoonejans, J., Vanacker, V., Opfergelt, S., Granet, M., & Chabaux, F. (2016). Coupling
750 uranium series and 10 Be cosmogenic radionuclides to evaluate steady-state soil
751 thickness in the Betic Cordillera. *Chemical Geology*.
752 Seret, G., Dricot, E., & Wansard, G. (1990). Evidence for an early glacial maximum in the
753 French Vosges during the last glacial cycle. *Nature*, *346*(6283), 453-456.
754 Siame, L., Bellier, O., Braucher, R., Sébrier, M., Cushing, M., Bourlès, D., & Yiou, F. (2004).
755 Local erosion rates versus active tectonics: cosmic ray exposure modelling in
756 Provence (south-east France). *Earth and Planetary Science Letters*, *220*(3), 345-364.
757 Small, E.E., Anderson, R.S., Hancock, G.S., 1999. Estimates of the rate of regolith production
758 using 10Be and 26Al from an alpine hillslope. Geomorphology 27, 131–150.
759 Stille P., Pourcelot L., Granet M., Pierret M.-C., Perrone Th, Morvan G., Chabaux F. (2011)
760 Deposition and migration of atmospheric Pb in soils from a forested silicate

761 catchment today and in the past (Strengbach case ; Vosges mountains) ; evidence
762 from 210Pb activities and Pb isotope ratios. Chem. Geol. 289,140-153 (2011), doi:
763 10.1016/j.chemgeo.2011.07.021
764 Viville, D., Chabaux, F., Stille, P., Pierret, M. C., & Gangloff, S. (2012). Erosion and weathering
765 fluxes in granitic basins: the example of the Strengbach catchment (Vosges massif,
766 eastern France). *Catena*, *92*, 122-129.
767 West, N., Kirby, E., Bierman, P., Slingerland, R., Ma, L., Rood, D., & Brantley, S. (2013).
768 Regolith production and transport at the Susquehanna Shale Hills Critical Zone
769 Observatory, part 2: insights from meteoric 10Be. *Journal of Geophysical Research:*
770 *Earth Surface*, *118*(3), 1877-1896.
771 WRB, 2006. International Union Soil Sciences Working Group WRB. 2006. World reference
772 base for soil resources 2006. World Soil Resources Reports No. 103. FAO, Rome
773

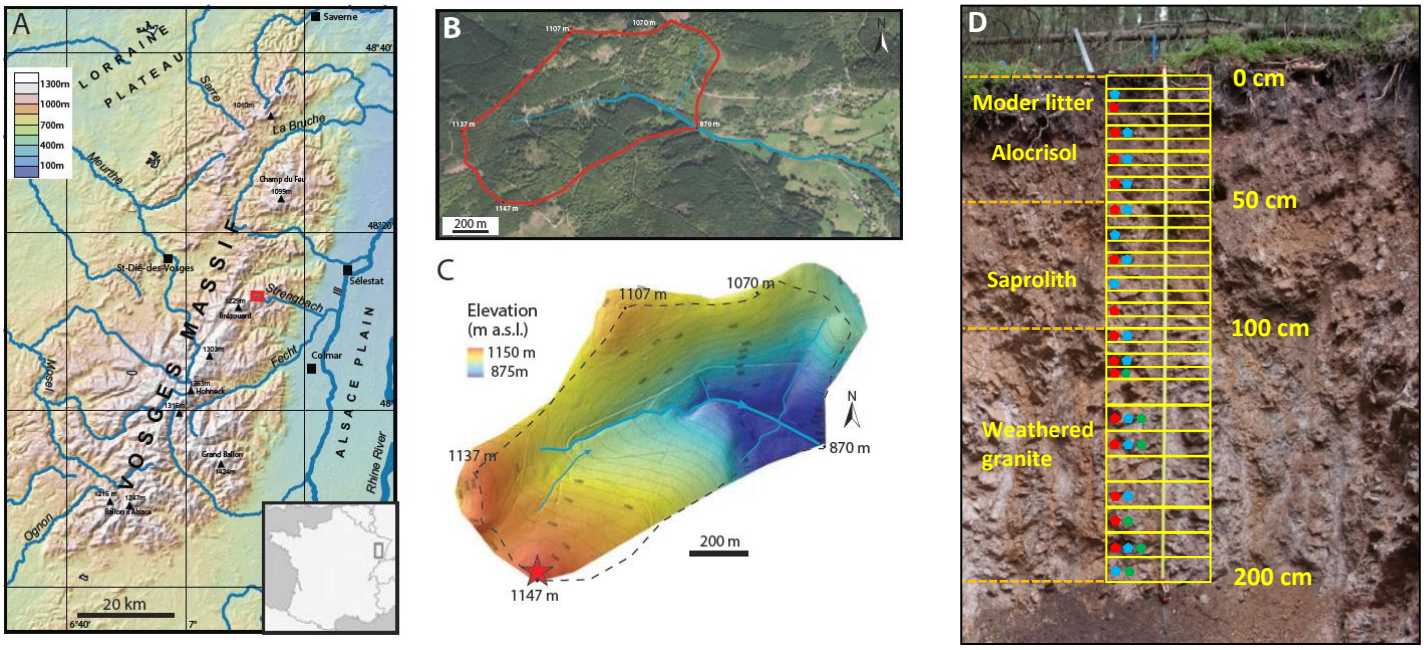


*Figure 1*

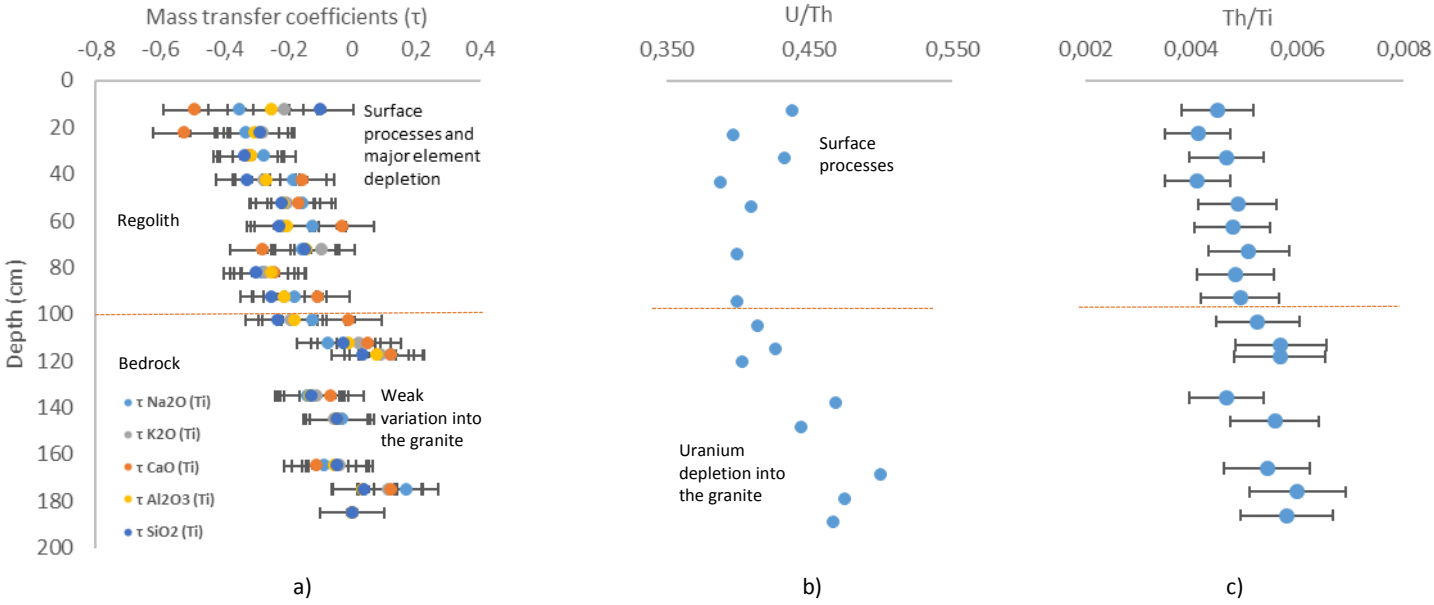


*Figure 2*

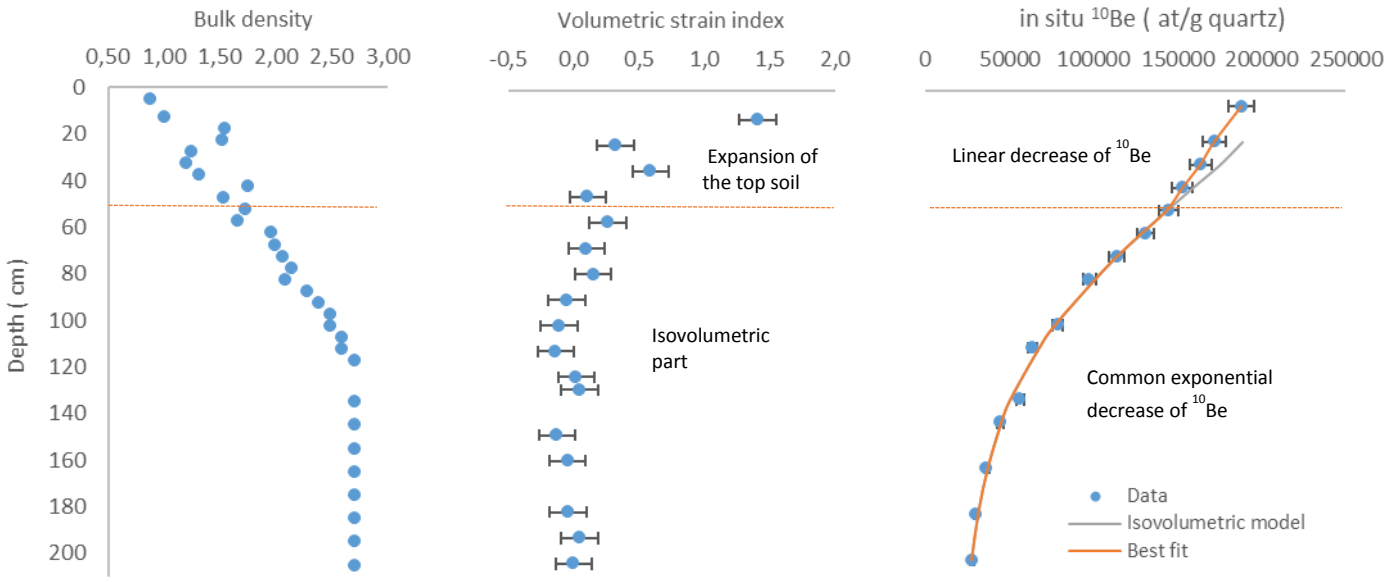


a) b) c)

*Figure 3*

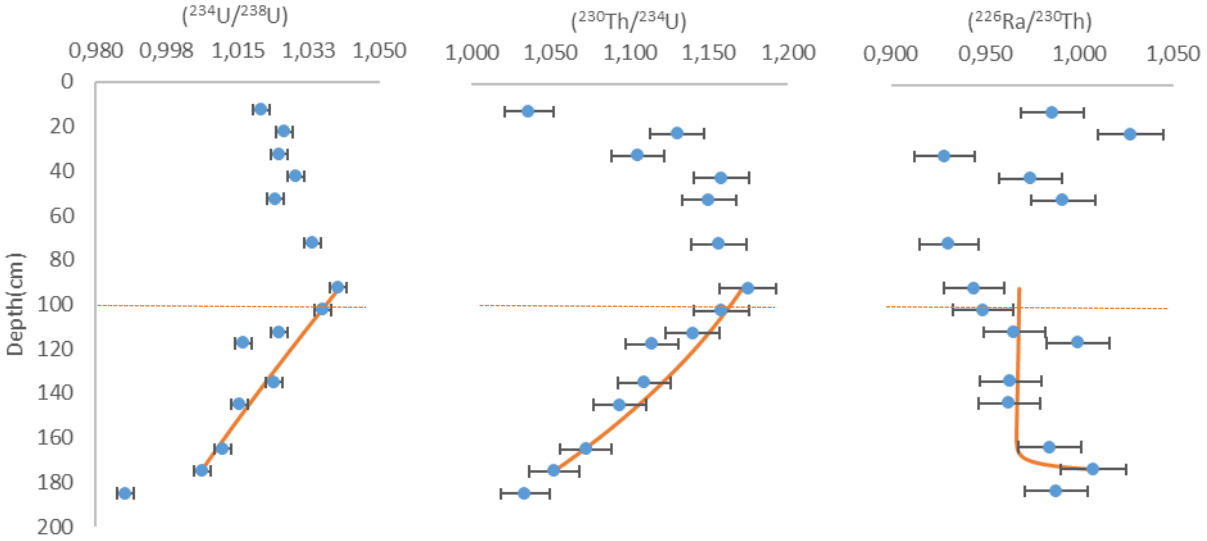


*Figure 4*

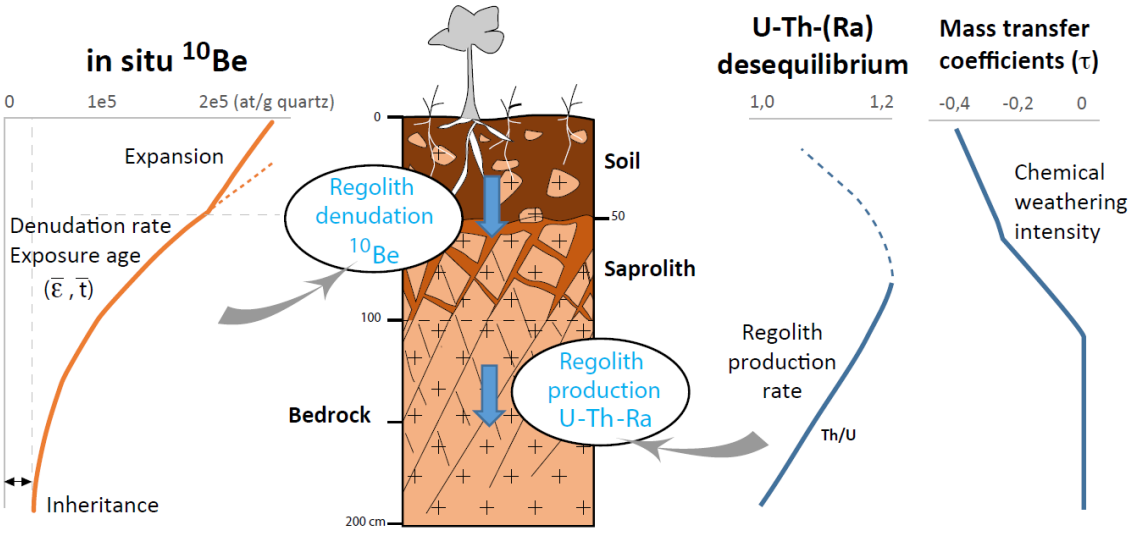
in situ 10Be
0
1e5
2e5 (at/g quartz)
Expansion
Denudation rate
Exposure age
(ε̄ , t̄)
Inheritance
Regolith denudation 10Be
Soil
Saprolith
Bedrock
Regolith production U-Th-Ra
0
50
100
200 cm
U-Th-(Ra) desequilibrium
1,0
1,2
Regolith production rate
Th/U
Mass transfer coefficients (τ)
-0,4
-0,2
0
Chemical weathering intensity

*Figure 5*

| Sample | Depth (cm) | Quartz (%) | Plagioclase Feldspars (%) | K-feldspars (%) | Micas and illites (%) | Kaolinite (%) | Interstratified clays (%) | Hematite (%) |
|---|---|---|---|---|---|---|---|---|
| STR13-41 | 12.5 | 43 | 17 | 25 | 8 | 2 | 5 | 0 |
| STR13-43 | 22.5 | 43 | 18 | 25 | 8 | 1 | 5 | 0 |
| STR13-45 | 32.5 | 40 | 20 | 23 | 9 | 2 | 6 | 0 |
| STR13-47 | 42.5 | 37 | 22 | 26 | 8 | 2 | 5 | 0 |
| STR13-49 | 52.5 | 38 | 18 | 31 | 9 | 3 | 1 | 0 |
| STR13-51 | 62.5 | 46 | 15 | 21 | 16 | 2 | 0 | 0 |
| STR13-53 | 72.5 | 48 | 15 | 18 | 17 | 2 | 0 | 0 |
| STR13-55 | 82.5 | 52 | 16 | 17 | 11 | 4 | 0 | 0 |
| STR13-57 | 92.5 | 45 | 16 | 22 | 15 | 2 | 0 | 0 |
| STR13-59 | 102.5 | 35 | 22 | 22 | 20 | 1 | 0 | 0 |
| STR13-61 | 112.5 | 34 | 20 | 26 | 19 | 0 | 0 | 1 |
| STR13-41B | 117.5 | 37 | 18 | 29 | 14 | 2 | 0 | 0 |
| STR13-42B | 135 | 40 | 22 | 22 | 13 | 2 | 0 | 1 |
| STR13-43B | 145 | 33 | 19 | 30 | 14 | 2 | 0 | 2 |
| STR13-45B | 165 | 37 | 22 | 28 | 11 | 2 | 0 | 0 |
| STR13-47B | 185 | 32 | 20 | 29 | 17 | 2 | 0 | 0 |

Table 1

| Sample | Depth (cm) | Type | Bulk density ($g/cm^3$) | $SiO_2$ (%) | $Al_2O_3$ (%) | CaO (%) | $Na_2O$ (%) | $K_2O$ (%) | MgO (%) | $Fe_2O_3$ (%) | MnO (%) | $TiO_2$ (%) | $P_2O_5$ (%) | LOI (1000 °C) (%) | Ta (ppm) | Zr (ppm) |
|---|---|---|---|---|---|---|---|---|---|---|---|---|---|---|---|---|
| STR13-41 | 12.5 | Soil | 1.0 | 73.20 | 12.05 | 0.16 | 1.70 | 4.55 | 0.21 | 1.30 | 0.011 | 0.18 | 0.27 | 4.79 | 2.3 | 81.0 |
| STR13-43 | 22.5 | Soil | 1.5 | 69.30 | 13.49 | 0.18 | 2.10 | 4.96 | 0.26 | 1.71 | 0.021 | 0.21 | 0.48 | 5.51 | 2.7 | 73.0 |
| STR13-45 | 32.5 | Soil | 1.2 | 68.50 | 14.03 | 0.27 | 2.40 | 4.99 | 0.32 | 1.69 | 0.027 | 0.22 | 0.59 | 4.85 | 2.9 | 70.0 |
| STR13-47 | 42.5 | Soil | 1.7 | 68.10 | 14.72 | 0.33 | 2.66 | 5.19 | 0.36 | 1.70 | 0.034 | 0.22 | 0.56 | 4.08 | 2.4 | 71.0 |
| STR13-49 | 52.5 | Soil | 1.7 | 70.20 | 13.99 | 0.29 | 2.45 | 5.09 | 0.30 | 1.53 | 0.032 | 0.20 | 0.50 | 3.22 | 2.7 | 67.0 |
| STR13-51 | 62.5 | Saprolite | 2.0 | 70.10 | 14.36 | 0.34 | 2.57 | 5.05 | 0.34 | 1.57 | 0.032 | 0.20 | 0.51 | 2.96 | 2.7 | 62.0 |
| STR13-53 | 72.5 | Saprolite | 2.1 | 70.60 | 14.08 | 0.23 | 2.25 | 5.30 | 0.26 | 1.59 | 0.030 | 0.18 | 0.41 | 2.52 | 2.7 | 62.0 |
| STR13-53[2] | 72.5 | Saprolite | 2.1 | 71.20 | 13.94 | 0.32 | 2.39 | 5.07 | 0.34 | 1.60 | 0.030 | 0.19 | 0.42 | - | - | - |
| STR13-53[3] | 72.5 | Saprolite | 2.1 | 70.70 | 13.77 | 0.34 | 2.47 | 5.09 | 0.34 | 1.58 | 0.030 | 0.18 | 0.42 | - | - | - |
| STR13-55 | 82.5 | Saprolite | 2.1 | 69.50 | 14.76 | 0.29 | 2.30 | 5.13 | 0.39 | 2.04 | 0.037 | 0.22 | 0.42 | 2.82 | 3.3 | 67.0 |
| STR13-57 | 92.5 | Saprolite | 2.4 | 69.60 | 14.56 | 0.32 | 2.45 | 5.18 | 0.39 | 2.08 | 0.028 | 0.20 | 0.35 | 2.39 | 3.1 | 61.0 |
| STR13-59 | 102.5 | Bedrock | 2.5 | 70.20 | 14.87 | 0.35 | 2.58 | 5.23 | 0.20 | 1.82 | 0.023 | 0.20 | 0.35 | 2.26 | 3.1 | 64.0 |
| STR13-61 | 112.5 | Bedrock | 2.6 | 71.80 | 14.50 | 0.30 | 2.20 | 5.34 | 0.20 | 1.38 | 0.020 | 0.16 | 0.39 | 2.17 | 2.8 | 67.0 |
| STR13-41B | 117.5 | Bedrock | 2.7 | 71.60 | 14.80 | 0.30 | 2.50 | 5.35 | 0.20 | 1.19 | 0.020 | 0.15 | 0.34 | 1.97 | 2.5 | 64.0 |
| STR13-42B | 135 | Bedrock | 2.7 | 72.60 | 14.30 | 0.30 | 2.30 | 5.23 | 0.25 | 1.31 | 0.022 | 0.18 | 0.31 | 1.87 | 2.6 | 67.0 |
| STR13-43B | 145 | Bedrock | 2.7 | 72.60 | 14.38 | 0.28 | 2.37 | 5.10 | 0.26 | 1.25 | 0.027 | 0.17 | 0.33 | 1.59 | 2.8 | 70.0 |
| STR13-45B | 165 | Bedrock | 2.7 | 72.10 | 14.19 | 0.26 | 2.22 | 5.16 | 0.20 | 1.41 | 0.032 | 0.16 | 0.31 | 1.83 | 2.6 | 77.0 |
| STR13-46B | 175 | Bedrock | 2.7 | 71.80 | 14.20 | 0.30 | 2.60 | 5.46 | 0.26 | 1.27 | 0.017 | 0.15 | 0.33 | 1.7 | 2.5 | 70.0 |
| STR13-47B | 185 | Bedrock | 2.7 | 72.40 | 14.38 | 0.28 | 2.33 | 5.13 | 0.39 | 1.16 | 0.016 | 0.16 | 0.32 | 1.57 | 2.7 | 69.0 |

Table 2

| Sample | Depth (cm) | U (ppm) | Th (ppm) | ($^{234}U/^{238}U$) | ($^{230}Th/^{232}Th$) | ($^{230}Th/^{234}U$) | ($^{226}Ra/^{230}Th$) |
|---|---|---|---|---|---|---|---|
| STR13-41 | 12.5 | 3.417 | 7.800 | 1.021 | 1.412 | 1.036 | 0.986 |
| STR13-43 | 22.5 | 3.621 | 8.904 | 1.026 | 1.433 | 1.130 | 1.027 |
| STR13-45 | 32.5 | 4.224 | 9.752 | 1.025 | 1.495 | 1.105 | 0.928 |
| STR13-47 | 42.5 | 3.830 | 9.636 | 1.029 | 1.440 | 1.158 | 0.974 |
| STR13-49 | 52.5 | 3.763 | 9.179 | 1.024 | 1.471 | 1.150 | 0.992 |
| STR13-53 | 72.5 | 3.528 | 8.622 | 1.034 | 1.486 | 1.156 | 0.931 |
| STR13-53[2] | 72.5 | 3.575 | 8.643 | 1.032 | 1.499 | 1.155 | 0.936 |
| STR13-53[3] | 72.5 | 3.462 | 8.699 | 1.034 | 1.454 | 1.162 | 0.936 |
| STR13-57 | 92.5 | 3.841 | 9.387 | 1.040 | 1.519 | 1.175 | 0.944 |
| STR13-59 | 102.5 | 4.155 | 9.810 | 1.036 | 1.544 | 1.158 | 0.949 |
| STR13-61 | 112.5 | 3.884 | 9.111 | 1.025 | 1.517 | 1.140 | 0.966 |
| STR13-41B | 117.5 | 3.531 | 8.753 | 1.016 | 1.392 | 1.114 | 0.999 |
| STR13-42B | 135 | 3.957 | 8.433 | 1.024 | 1.623 | 1.109 | 0.963 |
| STR13-43B | 145 | 4.294 | 9.659 | 1.015 | 1.504 | 1.094 | 0.963 |
| STR13-45B | 165 | 4.601 | 9.193 | 1.011 | 1.653 | 1.072 | 0.984 |
| STR13-46B | 175 | 4.470 | 9.415 | 1.006 | 1.531 | 1.052 | 1.008 |
| STR13-47B | 185 | 4.269 | 9.149 | 0.987 | 1.451 | 1.034 | 0.988 |

Table 3

| Sample | Depth (cm) | Integrated density ($g/cm^3$) | Mass of quartz (g) | Total $^{9}Be$ (mg) | $^{10}Be/^{9}Be$ | ± (%) | In situ $^{10}Be$ (at/g quartz) | ± (%) |
|---|---|---|---|---|---|---|---|---|
| STR11-3 | 7 | 0.88 | 25.02 | 0.477 | 1.47E-13 | 3.1 | 188144 | 3.5 |
| STR13-43 | 22.5 | 1.19 | 17.23 | 0.285 | 1.55E-13 | 3.4 | 171954 | 3.9 |
| STR13-45 | 32.5 | 1.20 | 19.72 | 0.293 | 1.65E-13 | 4.0 | 163601 | 4.5 |
| STR13-47 | 42.5 | 1.27 | 14.68 | 0.290 | 1.16E-13 | 3.9 | 153162 | 4.4 |
| STR13-49 | 52.5 | 1.34 | 22.54 | 0.287 | 1.70E-13 | 3.9 | 144995 | 4.4 |
| STR13-51 | 62.5 | 1.41 | 18.60 | 0.277 | 1.32E-13 | 3.3 | 131079 | 3.9 |
| STR13-53 | 72.5 | 1.49 | 23.79 | 0.281 | 1.45E-13 | 3.8 | 114030 | 4.3 |
| STR13-55 | 82.5 | 1.56 | 22.03 | 0.252 | 1.23E-13 | 3.2 | 97672 | 3.7 |
| STR13-59 | 102.5 | 1.73 | 22.45 | 0.303 | 8.75E-14 | 3.9 | 78918 | 4.4 |
| STR13-61 | 112.5 | 1.80 | 18.32 | 0.274 | 6.39E-14 | 4.0 | 63992 | 4.5 |
| STR13-42B | 135 | 1.96 | 29.31 | 0.291 | 8.49E-14 | 3.9 | 56360 | 4.4 |
| STR13-43B | 145 | 2.01 | 40.35 | 0.248 | 1.09E-13 | 5.2 | 44712 | 5.5 |
| STR13-45B | 165 | 2.09 | 38.00 | 0.278 | 7.48E-14 | 4.5 | 36532 | 4.9 |
| STR13-47B | 185 | 2.16 | 48.84 | 0.268 | 8.31E-14 | 3.9 | 30440 | 4.4 |
| STR13-49B | 205 | 2.21 | 57.09 | 0.280 | 8.55E-14 | 3.8 | 28057 | 4.3 |

Table 4

| Site | Regolith production from U-series data (T/km²/yr) | Regolith denudation from profile $^{10}$Be data (T/km²/yr) | Regolith denudation from river sediment $^{10}$Be data (T/km²/yr) | Erosion from river sediment load (T/km²/yr) |
|---|---|---|---|---|
| Strengbach Catchment (France) | 30 ± 10 (1) | 37 ± 15 (1) | - | 10 ± 2 (2) |
| Susquehanna Shale Hills Observatory (United States) | 29 ± 24 - 77 ± 20 (3) | 27 ± 10 - 34 ± 10 (4) | 39 (5) | - |
| Betic Range (Spain) | 12 ± 2 - 41 ± 9 (6) | 24 ± 5 - 39 ± 3 (6) | - | - |
| Nunnock Catchment (Australia) | 20 ± 3 - 130 ± 24 (7) | 12 ± 2 - 90 ± 5 (8) | 87 ± 9 (8) | - |
| Rio Icacos Watershed (Porto Rico) | 76 ± 20 (9) | 42 ± 15 - 85 ± 30 (10) | 73 ± 25 (10) | 300 (11) |

Table 5

**Mineralogical composition of the analyzed samples : methods and results**

The mineralogical compositions of all the powdered 250-µm bulk samples were determined by XRD with a Siemens D5000 diffractometer with scanning from 4 to 84°, a space step of 0.04° and a time step of 18 s. The <2-µm clay fractions were separated by centrifugation and analyzed after air drying and treatment with glycol ethylene and hydrazine to distinguish illites, smectites, kaolinites and inter-stratified clays. The quantitative estimation of the proportion of the different minerals has been performed by the Rietveld method with the Siroquant software. The analytical uncertainty is approximately 3 % for the mass fraction of quartz and plagioclase and 5 % for the mass fraction of micas and clays.

The whole rock XRD analyses (Table Table EA1) show that quartz is the most abundant primary mineral (32 to 48 %), followed by K-feldspar (17 to 31 %), plagioclase feldspar (15 to 22 %), biotite and muscovite (approximately 9 %). Clay minerals include illites, smectites, interstratified illites/smectites and kaolinites, with a bulk clay fraction from a few % in the bedrock to 10 % in the upper soil (Table 1). Thin section observations confirm the presence of the above primary minerals (quartz, K-feldspar, plagioclase feldspar, biotite, and muscovite) and also indicate the presence of apatite, zircon, small amounts of aluminum silicates, hematite and rutile.

***Table Caption***

*Table EA1 1*: Bulk X-ray diffraction analysis for the studied weathering profile.